Attitude Control for an Aero-Vehicle Using Vector Thrusting and Variable Speed Control Moment Gyros

Jong-Yeob Shin*
National Institute of Aerospace (N.I.A.), Hampton, VA 23666.
K.B Lim†and D.D. Moerder‡
NASA Langley Research Center, Hampton, VA 23681.

Abstract

Stabilization of passively unstable thrust-levitated vehicles can require significant control inputs. Although thrust vectoring is a straightforward choice for realizing these inputs, this may lead to difficulties discussed in the paper. This paper examines supplementing thrust vectoring with Variable-Speed Control Moment Gyroscopes (VSCMGs). The paper describes how to allocate VSCMGs and the vectored thrust mechanism for attitude stabilization in frequency domain and also shows trade-off between vectored thrust and VSCMGs. Using an H_2 control synthesis methodology in LMI optimization, a feedback control law is designed for a thrust-levitated research vehicle and is simulated with the full nonlinear model. It is demonstrated that VSCMGs can reduce the use of vectored thrust variation for stabilizing the hovering platform in the presence of strong wind gusts.

Nomenclature

Platform parameters

m: total mass.

$J(\eta)$: total inertia moment.

$I^a_{\gamma F}$: inertia moment of fan rotational parts about spin axis.

I^a_B: inertia moment of a momentum wheel about spin axis.

A: collection of prop spin unit vector components.

c: first moment of inertia of the total system.

*Staff Scientist, AIAA Member, j.y.shin@nianet.org
†Senior Researcher, Dynamics System and Control Branch, AIAA Member. k.b.lim@larc.nasa.gov
‡Senior Researcher, Dynamics System and Control Branch, AIAA Member. d.d.moerder@larc.nasa.gov

$C(\epsilon)$: Direction Cosine Matrix (DCM) from the inertia frame to the body frame

$T(\omega_s, \theta), \tau(\omega_s, \theta)$: net force and torque generated by four ducted fans

$\tau^c_{\omega_s}$: control torque for fan speed.

$\tau^c_{\Omega_B}$: control torque for a momentum wheel speed.

a_B: spin unit vector of a momentum wheel

Ω_B: Momentum wheel speed.

VSCMG parameters

τ_s, τ_g: wheel speed control torque and gimbal torque

I^s_C,I^o_C, I^g_C: total moment of inertia about spin axis, output axis, and gimbal axis.

I^s_ω: wheel inertia moment about spin axis.

I_{C_i}: total moment of inertia of the i-th VSCMG.

η_i: gimbal angle of the i-th VSCMG

$C^o_{G_i}$: the DCM from the body frame to the initial gimbal frame of the i-th VSCMG

$C_{G_i}(\eta_i)$: the DCM from the initial gimbal frame to the current gimbal frame of the i-th VSCMG

$$G(\eta): \begin{bmatrix} (sin(\eta_1) & 0 & cos(\eta_1))C^o_{G_1} \\ (sin(\eta_2) & 0 & cos(\eta_2))C^o_{G_2} \\ (sin(\eta_3) & 0 & cos(\eta_3))C^o_{G_3} \\ (sin(\eta_4) & 0 & cos(\eta_4))C^o_{G_4} \end{bmatrix}$$

$$K(\eta): \begin{bmatrix} (cos(\eta_1) & 0 & -sin(\eta_1))C^o_{G_1} \\ (cos(\eta_2) & 0 & -sin(\eta_2))C^o_{G_2} \\ (cos(\eta_3) & 0 & -sin(\eta_3))C^o_{G_3} \\ (cos(\eta_4) & 0 & -sin(\eta_4))C^o_{G_4} \end{bmatrix}$$

1 Introduction

Hovering vehicles levitated by vectored thrust systems frequently have their center of mass located above the point of application of the thrust vector, resulting in unstable or neutrally stable open-loop attitude dynamics. Such vehicles, and their stability characteristics, have attracted attention recently [1, 2, 3, 4, 5] for their suitability for a number of practical applications. A natural and conventional choice of control for stabilizing vehicle attitude is to actively vary the thrust vector. Particularly for small vehicles with low moments of inertia, however, the thrust vector correction necessary for stabilizing a passively unstable vehicle can be quite active, and may induce unsteady flow effects which are difficult to model. This difficulty is important because an unstable vehicle requires a high-performance control system which, in turn, requires an accurate model of the dynamics. This paper examines using Variable-Speed Control Moment Gyroscopes (VSCMGs) to, at least, partially take over the role of stabilization from thrust vectoring in these vehicles. These devices have the advantage that it is straightforward to accurately model their behavior. Additionally, by taking over a portion of the stabilization activity from the thrust vectoring system,

the amplitude and higher frequency content of the control from the latter can be reduced, making it, in turn, easier to model.

In Ref. [1], it has been suggested to enhance directional stability of the airframe by introducing an angular momentum bias generated using a momentum wheel. The approach can circumvent the problem of control-induced unsteady aerodynamics on the closed-loop stability during attitude stabilization. Detailed nonlinear simulations in Ref. [1] of the NASA Flying Test Platform (NFTP) under a strong wind gust condition showed the potential of the approach in terms of attitude robustness. In Ref. [2], the feasibility of using a set of VSCMGs was demonstrated to obtain controlled performance beyond what is possible through a bias momentum stability-enhanced system. Using a Lyapunov stability condition, a nonlinear control law was synthesized for the NFTP system which incorporates vector thrusting, a bias momentum wheel and VSCMGs and was simulated in the presence of strong wind gusts. The improved performance of the NFTP system using VSCMGs was demonstrated in Ref. [2].

This paper describes control allocation with VSCMGs and vectored thrust machinery in attitude stabilization of the NFTP. Since the VSCMGs can generate internal control torques to effectively and very reliably redistribute angular momentum to control the platform independently of ducted fan and control vane aerodynamics, they are assigned to generate control torque required for attitude stabilization of the platform in high frequency domain. The ducted fans with control vanes are assigned to stabilize the platform in low frequency domain in order to mitigate unpredictable unsteady aerodynamic phenomena. A feedback control law is synthesized minimizing H_2 norm of the system augmented with weighting functions. Nonlinear simulations demonstrate the trade-off of control efforts between VSCMGs and vectored thrust machinery (fan speed and control vanes).

This paper contains the following sections. In Section 2, NASA Flying Test Platform is described and equations of motion are derived to calculate the internal torque generated by VSCMGs and the effects on motion due to gimbal angle variation. In Section 3, the detailed control synthesis framework is described, which involves control allocations of VSCMGs and vector thrusting in the frequency domain. In Section 4, nonlinear simulation results are presented and this paper is concluded with a brief summary in Section 5.

2 NFTP Description and Equations of Motion

2.1 The NASA Flying Test Platform Description

The NFTP is a testbed for exploring combining thrust vectoring and internal angular momentum exchanges in unstable thrust-levitating vehicles. The system, pictured in Fig. 1, is levitated by thrust from four electric motors driving shrouded fans. Downstream of each fan are two thrust vectoring vanes for a total of eight vanes. All motors and vanes are independently controlled. The system is currently equipped with a flywheel, aligned with the vehicle's body vertical axis, that generates an internal angular momentum bias, but the vehicle is simulated with both the flywheel and a set of VSCMGs. The momentum wheel speed is regulated as constant with a simple PI feedback control law. The detailed physical parameters of the vehicle and the angular momentum bias are given in Ref. [2].

In this paper, four VSCMGs are included in the dynamics, configured in the pyramid shape in Ref. [6]. Each wheel inertia moment about spin axis is 0.005 Kg m^2 and the initial wheel speed

of each VSCMG is an user-selected parameter that scales the authority of the CMG systems. The initial speed is of importance, because it comprises a nominal "set point" in the control design, similar to the trim values of the propulsive control effectors. The total principal moment of inertia for each VSCMG is roughly

$$I_C = \text{diag}([I_C^s, I_C^o, I_C^g]) = \text{diag}([0.0053, 0.0026, 0.0026])(\text{Kg m}^2) \tag{1}$$

The output torque capacity of each VSCMG [2] is roughly 10 N-m with initial wheel speed 9000 rpm.

2.2 Equations of Motion

The equations of motion of the NFTP with four VSCMGs have been introduced in Ref. [1] with the following states: total linear momentum p, total angular momentum h, fan angular momentum along spin axis h_a, flying wheel angular momentum along spin axis h_{B_z}, VSCMG wheel angular momentum $h_{W.1}$ along spin axis and VSCMG angular momentum $h_{C.2}$ along gimbal axis. The total linear and angular momentum are difficult to be measured directly; therefore the equations of motion are rewritten in order to re-define states which can be measurable directly by physical sensors. The redefined states are as follows: platform velocity v, platform angular velocity ω, fan motor speed ω_s, momentum wheel speed Ω_B, VSCMG wheel speed Ω and gimbal angle rate $\dot{\eta}$.

From Ref. [1], the equations of motion in vectrix form are

$$\begin{Bmatrix} \dot{p} \\ \dot{h} \end{Bmatrix} = \begin{bmatrix} -\omega^\times & 0 \\ -v^\times & -\omega^\times \end{bmatrix} \begin{Bmatrix} p \\ h \end{Bmatrix} + \begin{bmatrix} mI_{3\times 3} \\ c^\times \end{bmatrix} C(\epsilon) g_o + \begin{Bmatrix} T(\omega_s, \theta) \\ \tau(\omega_s, \theta) \end{Bmatrix} + \begin{Bmatrix} f_{aero} \\ \tau_{aero} \end{Bmatrix} \tag{2}$$

$$\dot{h}_a = \tau_{_F}(\omega_s) + \tau_{\omega_s}^c \tag{3}$$

$$\dot{h}_{_{B_z}} = \tau_{_{B_z}}(\Omega_B) + \tau_{\Omega_B}^c \tag{4}$$

$$\begin{Bmatrix} \dot{h}_{W.1} \\ \dot{h}_{C.2} \end{Bmatrix} = \begin{Bmatrix} \tau_s \\ -\text{diag}(G(\eta)\omega)\left[(I_C^s - I_C^o)K(\eta)\omega + I_W^s \Omega\right] + \tau_g \end{Bmatrix} \tag{5}$$

The momenta are related to the velocities as follows

$$\begin{Bmatrix} p \\ h \\ h_{C.2} \\ h_{W.1} \\ h_a \\ h_{B_z} \end{Bmatrix} = \left[\begin{array}{c|c} M(\eta) & \Phi(\eta)^T \\ \hline \Phi(\eta) & \Psi \end{array}\right] \begin{Bmatrix} v \\ \omega \\ \dot{\eta} \\ \Omega \\ \omega_s \\ \Omega_B \end{Bmatrix} \tag{6}$$

where

$$M(\eta) \triangleq \begin{bmatrix} mI_{3\times 3} & -c^\times \\ c^\times & J(\eta) \end{bmatrix}, \tag{7}$$

$$\Phi(\eta) \triangleq \begin{bmatrix} 0_{4\times3} & I_C^g K_o \\ 0_{4\times3} & I_W^a K(\eta) \\ 0_{4\times3} & I_F^a A^T \\ 0_{1\times3} & I_B^a a_B^T \end{bmatrix} \tag{8}$$

$$\Psi \triangleq \text{diag}\left(I_C^g,\ I_W^a,\ I_{\gamma F}^a,\ I_B^a\right) \tag{9}$$

In general applications with VSCMGs such as attitude control of satellites in Refs. [7, 8, 9, 10], the change of the total moment inertia due to VSCMG gimbal angle variations are generally small enough to be ignored. In the NFTP, this assumption may be not hold. Note that the total moment of inertia J is a function of gimbal angle η in this paper and is written as

$$J(\eta) \triangleq J_o + \sum_{i=1}^{4} [C_{G_i}(\eta_i) C_{G_i}^o]^T I_{C_i} [C_{G_i}(\eta_i) C_{G_i}^o] \tag{10}$$

After algebraic manipulation of the time derivatives in Eq.(6), the equations of motion of the platform can be rewritten as follows:

$$\dot{x} = \bar{M}^{-1} G_f(x, \theta, \eta, \epsilon) + \bar{M}^{-1} U_1 \tag{11}$$

where $x = [v \ \ w \ \ \dot{\eta} \ \ \Omega \ \ \omega_s \ \ \Omega_B]^T$ and $U_1 = [0 \ \ \tau_g \ \ \tau_s \ \ \tau_{\omega_s}^c \ \ \tau_{\Omega_B}^c]^T$. The matrix $\bar{M}$ and function G_f are defined as follows:

$$\bar{M} \triangleq \left[\begin{array}{c|c} M(\eta) & \Phi(\eta)^T \\ \hline \Phi(\eta) & \Psi \end{array}\right] \tag{12}$$

$$G_f \triangleq \begin{bmatrix} \phi + \begin{Bmatrix} 0 \\ \tau_c \end{Bmatrix} + \begin{Bmatrix} T + f_{aero} \\ \tau + \tau_{aero} \end{Bmatrix} \\ -diag(G(\eta)\omega)\left[(I_C^s - I_C^o)K(\eta)\omega + I_W^a \Omega\right] \\ -I_W^a \dot{K}(\eta) w \\ \tau_{_F}(\omega_s) \\ \tau_{_{B_z}}(\Omega_B) \end{bmatrix} \tag{13}$$

The function ϕ is

$$\phi = \left(\begin{bmatrix} -w^\times & 0 \\ -v^\times & -w^\times \end{bmatrix} M - \begin{bmatrix} 0 & 0 \\ 0 & \frac{dJ(\eta)}{d\eta}\dot{\eta} \end{bmatrix} \right) \begin{Bmatrix} v \\ w \end{Bmatrix} + \begin{bmatrix} mI_{3\times3} \\ c^\times \end{bmatrix} C(\epsilon) g_o. \tag{14}$$

Note that the term $\frac{dJ(\eta)}{d\eta}\dot{\eta}$ appears in Eq.(14) since the total inertia moment is a function of VSCMG gimbal angle. The torque τ_c acting on the platform in Eq. (13) is

$$\tau_c = -w^\times (A I_{\gamma F}^a \omega_s + a I_B^a \Omega_B + K_o^T I_C^g \dot{\eta} + K(\eta)^T I_W^a \Omega) - \frac{dK(\eta)^T}{d\eta} \dot{\eta} I_W^a \Omega \tag{15}$$

From Eq.(15), it is observed the gyroscopic effect due to prop rotation, the moment wheel rotation, gimbal angle rate change, and VSCMG wheel rotation. The last term of Eq.(15) represents the

internal torque generated by the VSCMGs. In order to present the trade-off effects between vector thrusting and VSCMGs in attitude control for the platform, it is required that the internal torque is explicitly formulated in the equations of motion.

It is noticed that the matrix inversion of $\bar{M} \in \mathcal{R}^{19\times 19}$ at each time step is required to simulate the equations of motion of Eq.(11). It is not computationally tractable since the computation cost (memory and CPU time) of inverting large dimension matrices is high. Here, using the matrix inversion lemma [11], the matrix inversion is calculated by using matrix multiplications and the 3 by 3 matrix inversion at each time step, which is computationally tractable.

Kinematic equations of motion of the platform are written as

$$\dot{X}_i = C^T(\epsilon)v \tag{16}$$

$$\dot{\epsilon} = 0.5[0.5(1-\epsilon^T\epsilon)I_{3\times 3} + \epsilon^\times + \epsilon\epsilon^T]\omega \tag{17}$$

where ϵ is the Modified Rodrigues Parameters (MRP) [8, 9]. The direction cosine matrix $C(\epsilon)$ is

$$C(\epsilon) = I + \frac{4(1-|\epsilon|^2)}{(1+|\epsilon|^2)^2}\epsilon^\times + \frac{8}{(1+|\epsilon|^2)^2}\epsilon^\times\epsilon^\times. \tag{18}$$

2.3 Actuator Models

Based on bench test of a single representative ducted fan, the electric motor is modeled as

$$I_m\dot{\omega}_{s_i} = \tau_{_{F_i}}(\omega_{s_i}) + \tau^c_{\omega_{si}} = k_1\omega^2_{s_i} + k_2\omega_s + \tau^c_{\omega_{si}}(S_{PWM}) \tag{19}$$

where k_1 is an aero-drag coefficient due to prop rotation and k_2 is back EMF resistance coefficient due to armature rotation. Note that the control torque $\tau^c_{\omega_{si}}$ is a function of PWM signal (S_{PWM}) generated by the motor controller (Aveox SH 96 Motor controller). The dynamics of the electrical loop of the DC motor is fast enough to be ignored. To validate the model, step responses of fan speed with predicted step responses are plotted in Fig. 2. To model the servo motor (JRDS 8411), frequency sweep signals of vane angle commands are applied to the servo. Deflected angles are measured by potentiometers in analog signal. From the input and output data, frequency transfer functions are obtained by using MATLAB. The transfer functions are also calculated at different motor speeds and are fitted by the first order model. Hereafter, the servo model $\frac{20}{s+20}$ is used for control synthesis.

3 Control Synthesis Framework

In this section, a feedback control synthesis frame work for the flying platform described. The control objectives are to make the platform robustly stable and to minimize its attitude variations for hovering in the presence of wind gusts. The control design problem is formulated into minimizing the H_2 norm of weighted command-tracking errors and state variations with penalizing control actions shown in Fig. 3. An H_2 control law can be designed on a linearized model, which is calculated using Jacobian linearization around a given trim point. A trim condition at hovering is defined by setting state derivatives in Eq. (11) to zeros with additional parameter setting

$$\hat{v} = \hat{w} = \hat{\eta} = \hat{\dot{\eta}} = 0. \tag{20}$$

Here, $\hat{(\,)}$ notation denotes trim or nominal rotation speed in the case of CMG wheels. Note that trim condition can be satisfied at any gimbal angle of VSCMGs. Here, the trim gimbal angle is set to zero for convenience. It is possible to choose a trim gimbal angle based on controllability of VSCMG with the given VSCMG configuration. The details are, however, out of the scope of this paper.

To penalize state variations, performance weighting matrices W_p shown in Fig. 3 are defined as

$$W_p = \text{block diag}(1000I_{4\times4}, 0.1I_{4\times4}, 100I_{4\times4}) \tag{21}$$

to compensate different physical units of each state. In this design frame work, the states corresponding the weighting matrix W_p are $[\Omega \quad \omega_s \quad \dot{\eta}]$. The weighting matrix W_e to penalize the command tracking error signal in Fig. 3 is set to

$$W_e = \text{block diag}(0.1I_{3\times3}, 500I_{3\times3}, 2I_{3\times3}, 100I_{3\times3}). \tag{22}$$

For hovering, the commands of X, ϵ, V and ω are set as zero.

In this paper, an attitude control scheme with vectored thrust machinery and VSCMGs is posed in which VSCMGs generate internal control torque to stabilize the platform in high frequency domain and vectored thrust from ducted fans with control vanes generate torque to stabilize the platform in low frequency domain. The reason of two control actuators allocated in two frequency domains is to mitigate adverse unsteady aerodynamic effects that may be provided by rapid control vane motions in order to reject fast dynamic disturbance in the presence of strong wind gusts. In Ref. [1], it has been shown that rapid motion of control vane action is required to stabilize the platform under adverse weather condition without using VSCMGs and bias angular momentum. It was also shown that vane control authority was not enough to stabilize the platform under strong wind gusts in Ref. [1]. In order to allocate control actions of VSCMGs and vectored thrust machinery on each frequency domain, the weighting function W_{act} shown in Fig. 3 is defined as

$$W_{act} = \text{block diag}(\frac{0.01(s+1)}{s/500+1}I_{4\times4}, \frac{0.01(s+1)}{s/300+1}I_{4\times4}, \frac{10}{s/0.1+1}I_{4\times4}, 20I_{4\times4}) \tag{23}$$

where the entries in W_{act} correspond to the inputs, read from top to bottom. The frequency responses of the weighted function in the W_{act} block are shown in Fig. 4.

In this paper, the crossover frequency of the weighting function can be defined based on the mathematical model of the electric motor and the servo motor model. It, however, takes an important role in control allocation. The crossover frequency of each frequency weighting functions in Eq. (23) should be defined based on an unsteady aerodynamic effect bench test. In order to estimate the critical frequency of unpredicted aerodynamic force and moment generated by rapid control vane motion, a single shrouded prop unit has been bench-tested. Note that constant weight in the weighting function W_{act} on the VSCMG's wheel torque command is set in frequency domain for simplifying a control synthesis problem. After generating an augmented open loop system shown by the dashed in Fig. 3 with the given weighting functions, a feedback control synthesis problem is formulated in H_2 LMI optimization.

To investigate the effectiveness of VSCMGs in attitude control for the platform, feedback control laws are designed at different the wheel trim, or initial, speeds of the VSCMGs such as $\hat{\Omega} = 1000$, 2500, 5000, and 9000 (rpm), respectively, and the wheel speed of the momentum wheel is set as 2000 rpm.

4 NFTP Simulation Results

4.1 Wind Gust Disturbance Model

To simulate wind disturbances during hovering or low airspeed operations, crosswinds are assumed which impinge on a vertical cylinder attached to the upper part of the platform and which generate forces and moments via drag. The resulting aerodynamic drag on this cylindrical column is used to provide moment disturbances from the crosswind and turbulence impinging on the vehicle. The resulting disturbance model consists of forces and torques in the pitch and roll axis. The wind gust velocity is decomposed in two directions of pitch and roll axis. Each component of the wind gust is assumed to be independent and Gaussian with mean value (8 ft/sec) and standard deviation (50 ft/sec). To generate a colored gust model, the 3rd order low pass filter $(\frac{10}{0.001s^3 + 0.03s^2 + 0.03s + 1})$ is used. The disturbance force due to the wind gust is only assumed as the aerodynamic drag on the column with $C_D = 0.4$ at the Reynolds number $(5 \times 10^5 \sim 10^6)$. The disturbance torque is simply calculated as $\vec{l}_{a.c.} \times \vec{D}$ where $\vec{l}_{a.c}$ is a position vector to the aerodynamic center of the column from the platform C.G. The calculated disturbance force and torque acting on the platform is shown in Fig. 5 and are used for all simulations.

4.2 Simulation Results

In this section, simulation results based on the full nonlinear model with the feedback control laws designed based on each linearized model at different trim VSCMGs wheel speeds. In the full nonlinear model, a fan speed regulator is included and the momentum wheel speed is assumed to be constant as 2000 rpm for all simulations. In the following simulations, the aero-drag torque on the momentum wheel is ignored for convenience. The command signals for position, velocity, attitude angle and angular velocity of the platform are set to zero for hovering under the wind gust disturbance acting after 1 sec in all simulations. The attitude responses of the platform are shown in Fig. 6 for the case: $\hat{\Omega} = 1000$ rpm and Fig. 7 for the cases: $\hat{\Omega} = 2500$, 5000, and 9000 rpm. The plots in Fig. 6 and 7 imply that VSCMG actuators reduce Euler angle response effectively. It is observed from Figs. 6 and 7 that the attitude variations are smaller with faster wheel speed of VSCMGs since fast wheel speed of VSCMGs can generate large internal control torque on the platform. The vane deflection, fan speed, VSCMG gimbal angle responses, and VSCMG wheel speed responses are shown in Figs. 8 through 12, to compare control efforts for each case. From the plots in Figs. 8 and 9, it is observed that the control effort of fan speed and vane deflection can be reduced by increasing VSCMG control efforts. Note, from Figs. 9 and 10, that larger values of wheel speed $\hat{\Omega}$ in the VSCMGs reduced the gimbal angle variations and thrust vector angles needed for stability. Notice in Figs. 11 and 12 that the VSCMG Ω variations are less than 1.6 % of the initial wheel speed for all cases. It is also observed that the fast wheel speed (9000 rpm) requires smallest variations of the wheel speed during simulation for holding attitude.

From the simulation results, it is also observed that the RMS (Root Mean Square) Euler angle responses decrease as VSCMG $\hat{\Omega}$ values increase. To describe the trade-off of control efforts between vectored thrust (fan speed and vane deflection angle) and VSCMGs, the RMS time responses gimbal torque, gimbal angle rate, fan speed, wheel speed and vane deflection are shown in Figs. 13 and 14. It is observed from Figs. 13 and 14 that control action of vector thrust machinery (RMS of fan

speed and vane deflection angles) decreased as action of VSCMGs (RMS gimbal torque command) increase. Also, notice that fast wheel speed VSCMGs require small gimbal angle rate variation at constant gimbal torque. It corresponds to the fact that the internal control torque acting to the platform is proportional to the product of wheel speed and gimbal angle rate.

5 Conclusion

This paper has described attitude control using VSCMGs and vectored thrust machinery in the presence of strong wind gusts demonstrated on an experimental testbed, the NFTP. A feedback control law for the NFTP has been designed by minimizing H_2 norm with weighting functions which penalize the use of vectored thrust in high frequency domain to mitigate unsteady aerodynamic phenomena generated by rapid control vane motions. The required control torque for attitude stabilization in high frequency domain can be generated by the VSCMGs. Simulation results show the trade-off control effects between VSCMGs and vectored thrust for the NFTP with different VSCMG wheel speed levels. For the practical use of VSCMGs on aero-vehicles, the performance requirement under given environment is required to size VSCMGs.

Acknowledgments

This research of the first author's work was supported by National Aeronautics and Space Administration under NASA Contract No. NAS1-02117. The authors thank their colleagues Elvin Ahl and Jeffrey Massie for constructing the NFTP frame, and David Cox and Mario Smith for setting the bench test of the single ducted fan.

References

[1] Lim, K.B., Shin, J.-Y., Moerder, D.D., and Cooper, E.G., "A New Approach to Attitude Stability and Control for Low Airspeed Vehicles," in *AIAA Guidance, Navigation, and Control Conference and Exhibit*, (Providence, R.I.), August, 16-19 2004. AIAA Paper 2004-5008.

[2] Lim, K.B., Shin, J-Y., and Moerder, D.D., "Variable Speed CMG Control of A Dual-Spin Stabilized Unconventional VTOL Air Vehicle," in *AIAA 3rd Unmanned Unlimited Technical Conference, Workshop and Exhibit*, (Chicago, IL), September, 20-23 2004. AIAA 2004-6537.

[3] *Army Aerial and Joint Services VTOL Rotocraft Goverment/Industry/Academia Workshop*, (Williamsburg, VA), January, 27-29 2004.

[4] Fleming, J., Jones, T., Gelhausen, P., and Enns, D., "Improving Control System Effectiveness for Ducted Fan VTOL UAVs Operating in Crosswinds," in *AIAA 2nd Unmanned Unlimited Systems, Technologies, and Operations*, (San Diego, CA), September, 15-18 2003. AIAA 2003-6514.

[5] Lim, K.B., Shin, J.-Y., Cooper, E.G., Moerder, D.D., Khong, T.H., and Smith, M.F., "An Overview of The NASA Flying Test Platform Research," in *AIAA Guidance, Navigation, and Control Conference and Exhibit*, (Austin, TX), August, 11-14 2003. AIAA 2003-5775.

[6] Yoon, H. and Tsiotras, P., "Singularity Analysis of Variable-Speed Control Moment Gyros," *Journal of Guidance, Control, and Dynamics*, Vol. 27, No. 3, 2004, pp. 374–386.

[7] Hughes, P.C., *Spacecraft Attitude Dynamics*, ch. Cp.3. New York: John Wiley and Sons, 1986.

[8] Tsiotras, P., "Stabilization and Optimality Results for the Attitude Control Problem," *Journal of Guidance, Control, and Dynamics*, Vol. 19, No. 4, 1996, pp. 772–779.

[9] Schaub, H., Vadali, S.R., and Junkins, J.L., "Feedback Control Law for Variable Speed Control Moment Gyros," *Journal of the Astronautical Sciences*, Vol. 46, No. 3, 1998, pp. 307–328.

[10] Wie, B., *Spacecraft Vehicle Dynamics and Control*. AIAA Education Series, Reston, VA: AIAA Inc., 1998.

[11] Zhou, K., Doyle, J., and Glover, K., *Robust and Optimal Control*. New Jersey: Prentice Hall, 1996.

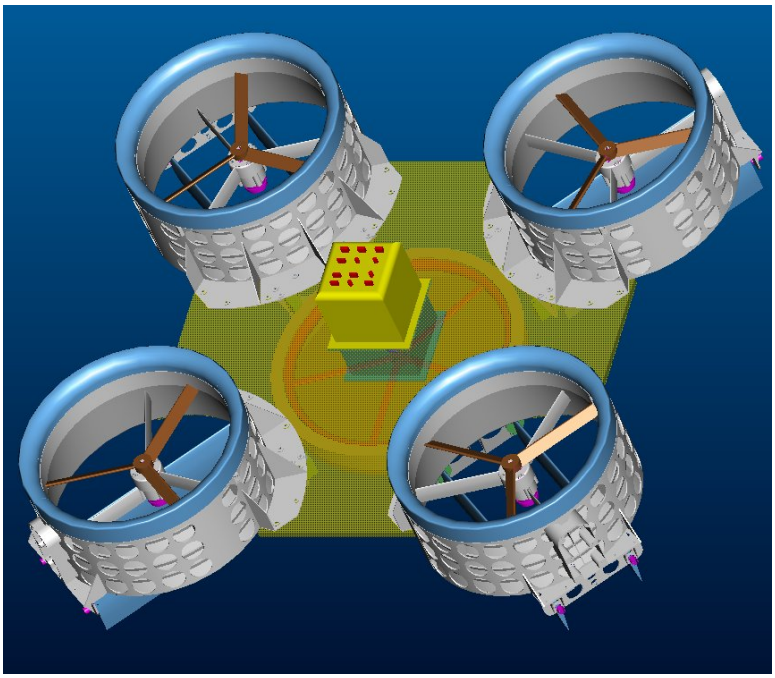

Figure 1: NASA Flying Test Platform

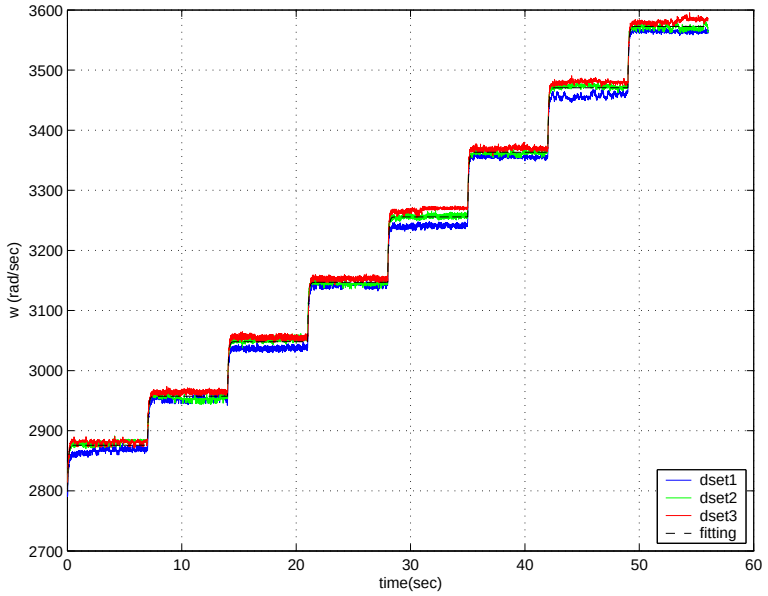

Figure 2: Measured fan speed step responses and predicted fan speed responses (dashed line) by the mathematical model.

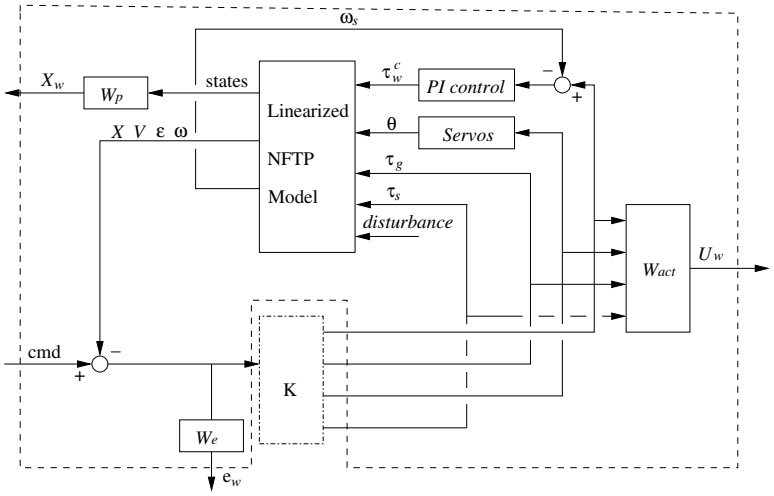

Figure 3: Control synthesis interconnection

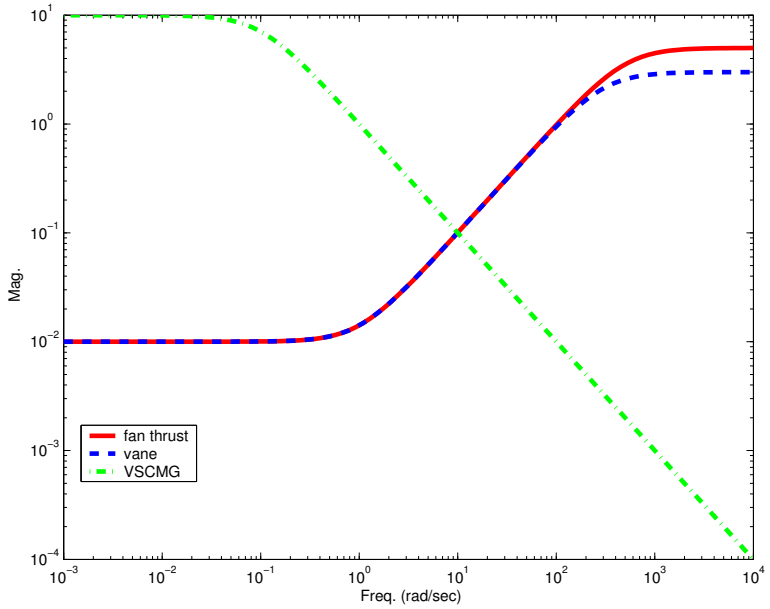

Figure 4: Weighting functions on fan thrust, vane angle, and gimbal torque commands.

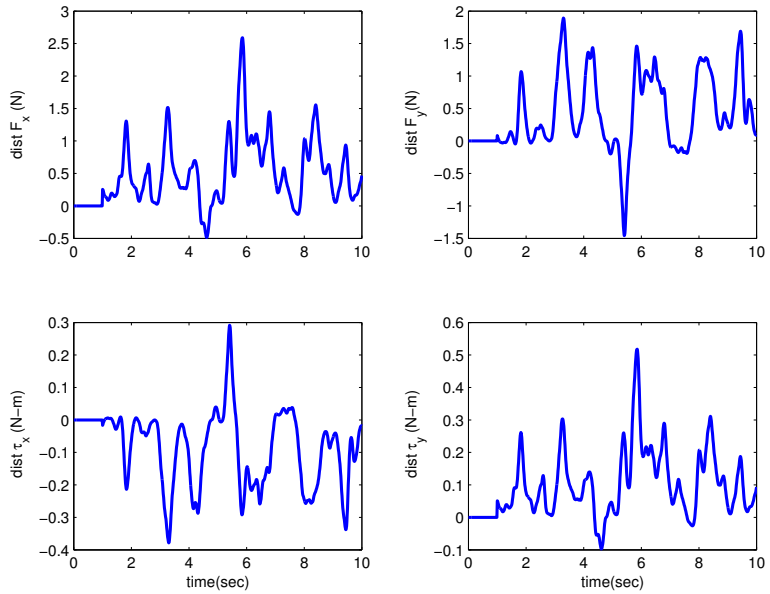

Figure 5: Disturbance forces and moments due to the wind gust.

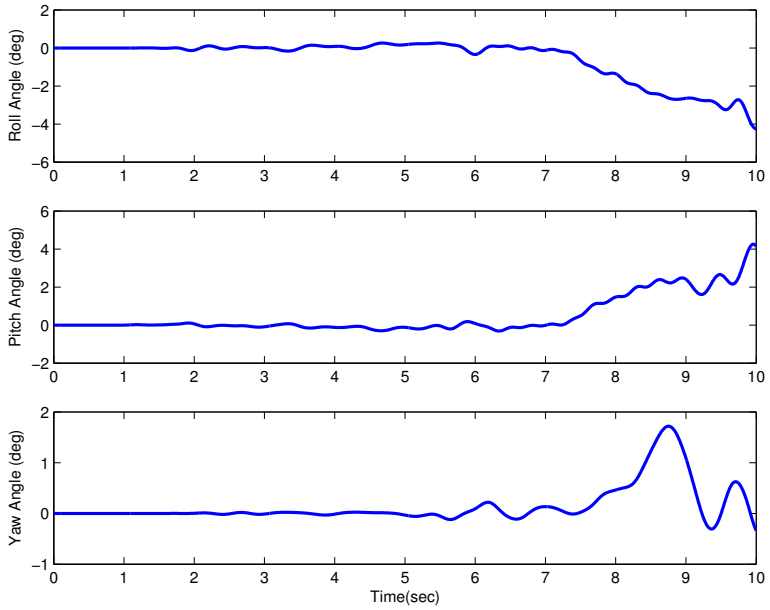

Figure 6: Euler angle responses with the nominal VSVMG wheel speed (1000 rpm).

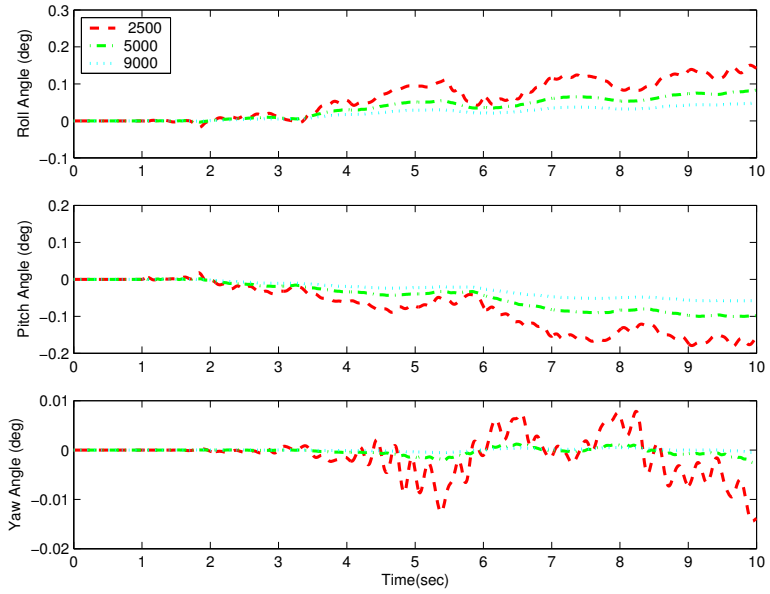

Figure 7: Euler angle responses with different initial VSCMG wheel speeds.

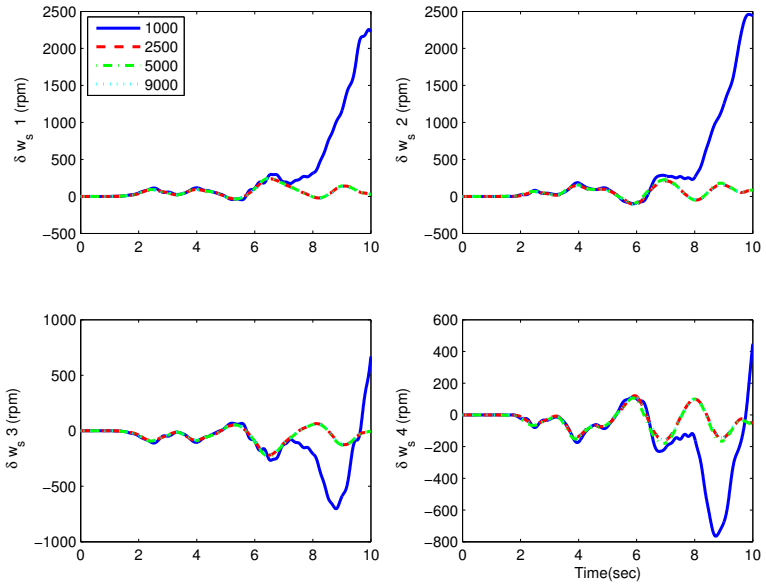

Figure 8: Incremental fan speed responses.

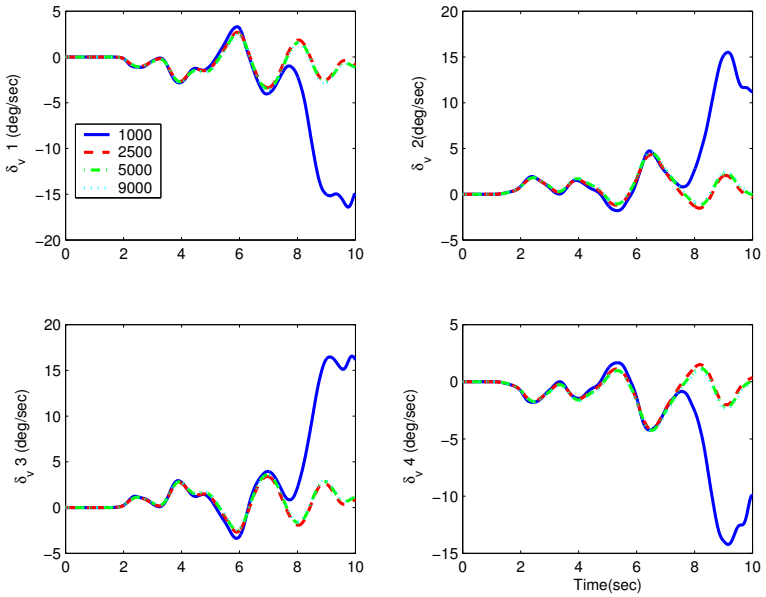

Figure 9: Vane deflection angle responses

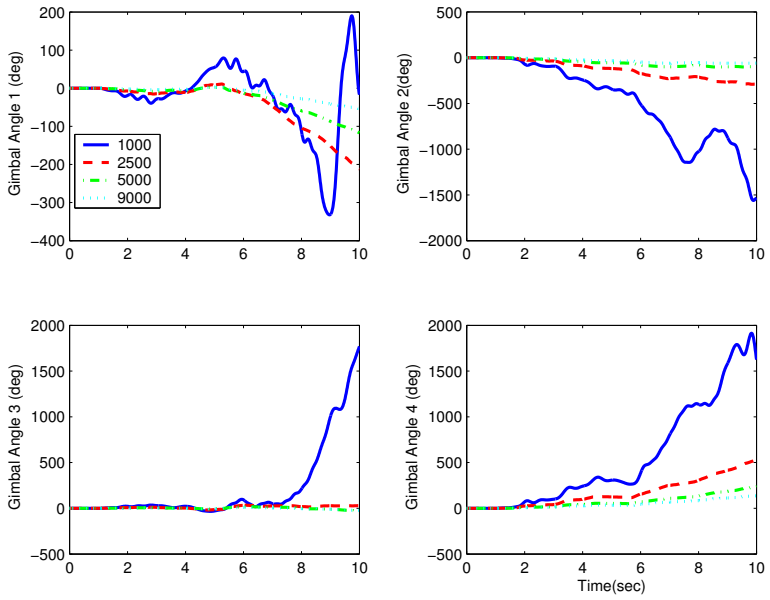

Figure 10: Gimbal angle responses.

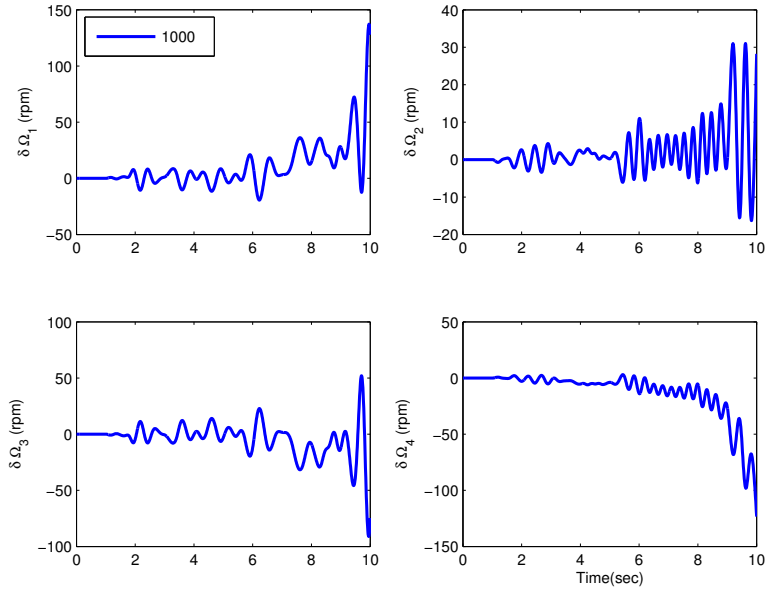

Figure 11: VSCMG wheel speed responses at $\hat{\Omega}$ 1000 rpm.

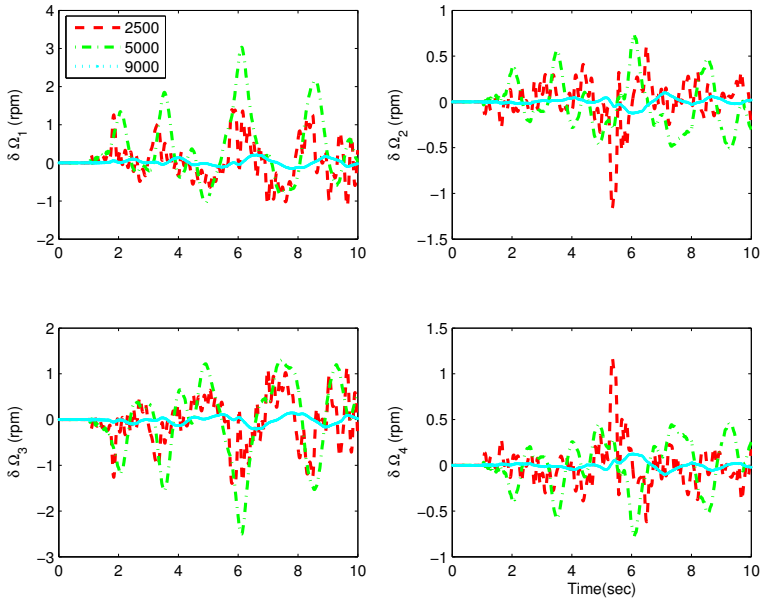

Figure 12: VSCMG wheel speed responses at $\hat{\Omega} = 2500,\ \ 6000,\ \ 9000$ rpm.

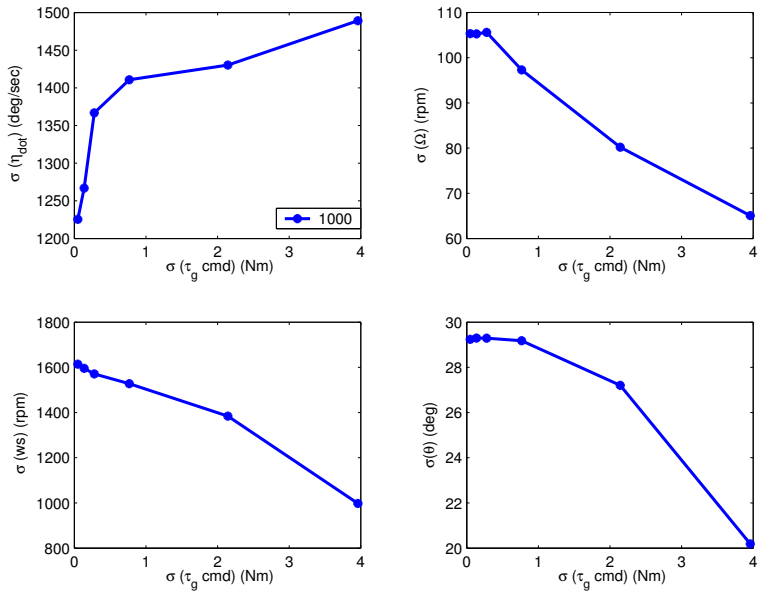

Figure 13: RMS of gimbal angle, wheel speed, fan speed and vane deflection angle at 1000 rpm initial wheel speed.

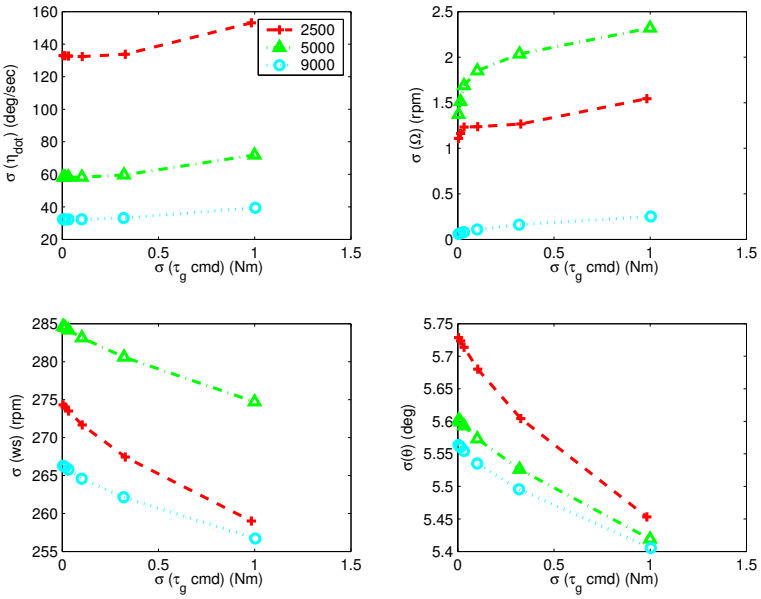

Figure 14: RMS of gimbal angle, wheel speed, fan speed and vane deflection angle.